AIAA JOURNAL
Vol. 32, No. 12, December 1994

Hypersonic Flow Past Open Cavities

Algacyr Morgenstern Jr.* and Ndaona Chokani†
North Carolina State University, Raleigh, North Carolina 27695

The hypersonic flow over a cavity is investigated. The time-dependent compressible Navier–Stokes equations are numerically solved. An implicit algorithm, with a subiteration procedure to recover time accuracy, is used to perform the time-accurate computations. The objective of the study is to investigate the effects of Reynolds number and cavity dimensions. The comparison of the computations with available experimental data, in terms of time mean static pressure, heat transfer, and Mach number, show good agreement. In the computations large vortex structures, which adversely affect the cavity flow characteristics, are observed at the rear of the cavity. A self-sustained oscillatory motion occurs within the cavity over a range of Reynolds number and cavity dimensions. The frequency spectra of the oscillations show good agreement with a modified semiempirical relation.

Introduction

THE presence of cavities in modern aerodynamic configurations occurs as a desired or undesired design feature, such as an internal stores carriage on an aircraft or an external rifling on a sabot launched projectile. Extensive experimental and analytical studies have shown that the flow past cavities experiences self-sustained oscillations over a wide range of flow conditions, from low subsonic speeds to supersonic speeds. These studies demonstrated that the oscillatory flow over cavities can affect the aerodynamic characteristics of the configuration rather adversely. With the present interest in developing an aerospace vehicle to travel at hypersonic speeds that may be required to perform store releases at these hypersonic speeds, a better understanding of the hypersonic flow over cavities is necessary. Although there have been considerable theoretical and experimental works conducted to understand the steady aspects of the severe aerothermodynamic environment associated with the hypersonic flow, there is little understanding of unsteady hypersonic aerodynamics. The large heat loads typical of steady hypersonic flight influence very strongly the vehicle's design. In addition, a strong coupling exists between the surface properties and the aerothermodynamic phenomena. The basic problems associated with the intense aerodynamic and thermal environment, observed in steady hypersonic flow, remain of fundamental concern in the unsteady flow, but an important consideration is also their effect on the unsteady, oscillatory character of the cavity flow.

Previous experiments, Nestler et al.[1] and Hahn,[2] have reported only mean flow measurements and have not addressed the unsteady flow characteristics. The analytical methods developed in the past[3] do not resolve sufficient details of the flowfield to provide any physical insight into the nature of the flow interactions. Computational fluid dynamics, on the other hand, has the potential to answer many of the issues associated with the unsteady hypersonic cavity flowfields. However, the explicit-type, numerical methods[4,5] previously used to study cavity flowfields are such that the magnitude of the time step used is restricted by the numerics of the computational scheme and not by the physics of the flow being solved. Since the maximum time step allowable by the numerics may be an order of magnitude or two smaller than the minimum time step of interest for the flow physics, the cost of the required computations can be prohibitively large and not suited to the conduct of parametric studies.

Presented as Paper 93-2969 at the AIAA 24th Fluid Dynamics Conference, Orlando, FL, July 6–9, 1993; received Dec. 20, 1993; revision received June 14, 1994; accepted for publication June 14, 1994.

*Graduate Student, Department of Mechanical and Aerospace Engineering. Student Member AIAA.

†Associate Professor, Department of Mechanical and Aerospace Engineering. Member AIAA.

This difficulty may be resolved through the use of an implicit-type numerical method. Implicit numerical methods to solve the Navier–Stokes equations for steady compressible flows have been reported by a number of researchers. However, these implicit methods have not been widely applied to unsteady compressible flows. In the present work, an implicit numerical algorithm, based on three-dimensional numerical method of Yoon and Kwak,[6] which has been successfully applied to numerous steady, viscous, turbulent, compressible flows was developed. This algorithm is second-order accurate in both space and time for steady-state calculations and has a highly efficient structure, which renders CPU speeds comparable to that of explicit schemes. However, to achieve this numerical efficiency, an explicit treatment is applied to the linearization of the viscous fluxes, that is, the viscous terms are time lagged. Moreover, an approximation in the factorization scheme compromises the time accuracy of the algorithm even more. In steady flow calculations these approximations are not a reason for concern, since at convergence all of the errors due to the cited approximations are zero. However, for unsteady flow computations, the time accuracy reduced due to the linearization and factorization approximations must be recovered.

Various authors have reported the use of a Newton-like subiteration procedure to increase time accuracy and rate of convergence of the numerical algorithm. The subiteration procedure is performed in a pseudotime level for each physical time step until convergence for that physical time step is achieved. Matsuno[7] presented a general formulation for time-accurate schemes that makes use of the Newton-like subiteration procedure, termed δ^{κ} form, that is κth-order accurate in time. Rogers et al.[8] used a Newton-like subiteration algorithm to compute steady and unsteady solutions of the incompressible Navier–Stokes equations. Simpson and Whitfield[9] used Newton-like subiterations in a flux-difference algorithm to compute unsteady solutions of the thin-layer Navier–Stokes equations. In the present work a Newton-like subiteration procedure is implemented to recover the time accuracy of the algorithm when applied to unsteady problems.

In this paper, the numerical algorithm was applied to study the nonreacting hypersonic laminar/transitional flow past a cavity. The computational results are compared with available time-mean experimental data for the geometries and flow conditions modeled here. The time-accurate computations reveal self-sustained oscillations not observed in the experiments. The frequency of oscillations agrees well with semiempirical predictions. In the following section, the computational techniques used are outlined. Then the validation of the numerical method with steady and nonsteady test cases is presented. A detailed study of the hypersonic cavity flowfield is then reported. Finally, the conclusions and future work are discussed.

Mathematical Formulation

The two-dimensional, unsteady, compressible, hypersonic flow past cavities is governed, as a first approximation, by the nonreacting

Navier–Stokes equations. In conservation law form and in a generalized curvilinear coordinate system (ξ, η), they may be written as

$$\frac{\partial \hat{Q}}{\partial t} + \frac{\partial(\hat{F} - \hat{F}_v)}{\partial \xi} + \frac{\partial(\hat{G} - \hat{G}_v)}{\partial \eta} = 0 \tag{1}$$

where Q is the unknown vector, $\hat{F}$ and $\hat{F}_v$ are the inviscid and viscous fluxes in the ξ direction, and $\hat{G}$ and $\hat{G}_v$ are the similar fluxes in the η direction.

Numerical Algorithm

The present time-accurate numerical method is based on the observation[7] that a δ form of the governing unsteady equations may be constructed with various combinations of the flux formulas and their Jacobians through the use of Newton-like subiterations. Furthermore, a suitable choice of the factorization procedure yields a scheme with fast convergence and low computational time per iteration.

Equation (1) can be written in difference form as

$$[(3/2)I + \Delta t(D_\xi \hat{A}\cdot + D_\eta \hat{B}\cdot)]\delta\hat{Q}^n = \tfrac{1}{2}\delta\hat{Q}^{n-1} - \Delta t\left[D_\xi\left(\hat{F}^n - \hat{F}_v^n\right) + D_\eta\left(\hat{G}^n - \hat{G}_v^n\right)\right] \tag{2}$$

where a second-order accurate Euler three-point backward time discretization is used. The inviscid and viscous fluxes are linearized by

$$\hat{F}^{n+1} = \hat{F}^n + \hat{A}\Delta\hat{Q}^n, \qquad \hat{F}_v^{n+1} = \hat{F}_v^n$$

where the inviscid flux Jacobian matrix is defined as

$$\hat{A} = \frac{\partial \hat{F}}{\partial \hat{Q}}$$

and $\hat{G}$, $\hat{G}_v$, and $\hat{B}$ are similarly defined.

A finite volume approach is used in the treatment of the spatial discretization of the fluxes. Second-order central differences are used in the left-hand side. A fourth-order artificial dissipation is added to the right-hand side (RHS) to control the undesired effect of the odd and even point decoupling characteristic of central differences.

In the present two-dimensional algorithm, the lower-upper symmetric-Gauss-Seidel factorization scheme proposed by Yoon and Kwak[6] is used. The advantage of this factorization is that the construction of the diagonal of the L and U matrices permits a scalar inversion, leading to a very efficient and vectorizable algorithm. The Jacobian matrix $\hat{A} = \hat{A}^+ + \hat{A}^-$ is approximated by

$$\hat{A}^\pm = \tfrac{1}{2}[\hat{A} \pm \rho(\hat{A})]$$

where

$$\rho(\hat{A}) = \max[|\lambda(\hat{A})|]$$

and $\lambda(\hat{A})$ is the eigenvalue of the Jacobian matrix $\hat{A}$. A similar procedure is applied to the Jacobian matrix $\hat{B}$.

With these approximations the factorization matrices are given by

$$L = [(3/2) + \Delta t\rho]I - \Delta t(\hat{A}^+_{i-1,j} + \hat{B}^+_{i,j-1})$$

$$D = [(3/2) + \Delta t\rho]I$$

$$U = [(3/2) + \Delta t\rho]I + \Delta t(\hat{A}^-_{i+1,j} + \hat{B}^-_{i,j+1})$$

where

$$\rho = \rho(\hat{A}) + \rho(\hat{B})$$

Equation (2) can thus be written as

$$LD^{-1}U\delta\hat{Q}^n = \text{RHS [Eq. (2)]} \tag{3}$$

The solution is then obtained in three steps as follows:

$$\begin{aligned} \delta\hat{Q}^* &= L^{-1}\text{RHS} \\ \delta\hat{Q}^{**} &= D\delta\hat{Q}^* \\ \delta\hat{Q}^n &= U^{-1}\delta\hat{Q}^{**} \end{aligned} \tag{4}$$

Subiteration Procedure

The preceding algorithm has given good results for steady flow calculations, see Yoon and Kwak.[6] However, for unsteady flow calculations the approximation of the flux Jacobian matrices and the linearization procedure reduce the accuracy of the time discretization. To overcome this difficulty a procedure presented in Matsuno[7] is introduced. At each time step a Newton-like iteration procedure is performed until convergence is achieved for each time step, while maintaining the unsteady form of the governing equations in the RHS of the algorithm. The idea of subiterations is that the governing equations may be iterated in pseudotime for each physical time step. At convergence of the pseudotime iterations (subiterations), the linearization and factorization errors go to zero, and the full temporal accuracy of the numerical discretization is recovered. This can be obtained by adding a pseudotime derivative[8] of the dependent variable vector to Eq. (1), which may be written as

$$\frac{\partial \hat{Q}}{\partial \tau} + \frac{\partial \hat{Q}}{\partial t} + \frac{\partial(\hat{F} - \hat{F}_v)}{\partial \xi} + \frac{\partial(\hat{G} - \hat{G}_v)}{\partial \eta} = 0 \tag{5}$$

where τ is a pseudotime variable that bears no relation with the physical time t. The finite difference form of Eq. (5) is obtained in a similar manner to that of Eq. (2). Using a backward first-order accurate time-difference formula to discretize the pseudotime derivative and applying an Euler implicit scheme at the $(n + 1)$ time level, it may be written as

$$[(3/2)I + \Delta t(D_\xi \hat{A}\cdot + D_\eta \hat{B}\cdot)]\delta\hat{Q}^{n,m} = -(3/2)(\hat{Q}^{n,m} - \hat{Q}^n) + \text{RHS [Eq. (2)]} \quad m = 0, 1, 2, 3, \ldots \tag{6}$$

where the pseudotime increment was assumed very large, and m denotes the pseudotime level. For $m = 0$, $\hat{Q}^m = \hat{Q}^n$, and the algorithm reduces to the steady-state formulation of Yoon and Kwak.[6] At convergence of the subiteration procedure $\delta\hat{Q}^{n,m} \to 0$, and the accuracy of the solution at each time step is the accuracy of the discretized unsteady governing equations.

Results and Discussion

The main objective of this work is to study the unsteady, compressible, viscous, hypersonic flow past cavities. The capability of the present numerical method to compute these complex flows was validated by first computing several test cases. The test cases presented here include the inviscid supersonic flow over a 20-deg compression ramp, the laminar supersonic flow over a flat plate, and the shock tube problem. The hypersonic flow over cavities was then investigated.

The computations were performed on a Cray Y-MP computer. A multiblock strategy was employed in the cavity flow studies to efficiently utilize the computer memory. The computational rate of the code was 4.7×10^{-6} CPU s/grid point/iteration, without any subiteration, and 7.0×10^{-6} CPU s/grid point/iteration, with one subiteration. No Courant-Friedrichs-Lewy (CFL) stability requirement was encountered in computing the test cases or cavity flows; CFLs up to 200 were routinely achievable. However, for the cavity flows, the time step was fixed to resolve the frequencies of interest in a time-accurate manner. For the unsteady cavity flows, once the initial transients were purged, data was acquired for purposes of spectral analysis. A maximum entropy method[10] for spectral estimation was applied. An attribute of the method was that exceedingly short data lengths, even less than the period of the lowest frequency of interest, are required to yield spectra. This further reduced the necessary computer time required to analyze unsteady flows. To the authors' knowledge this is the first application of the maximum entropy method to unsteady CFD analysis.

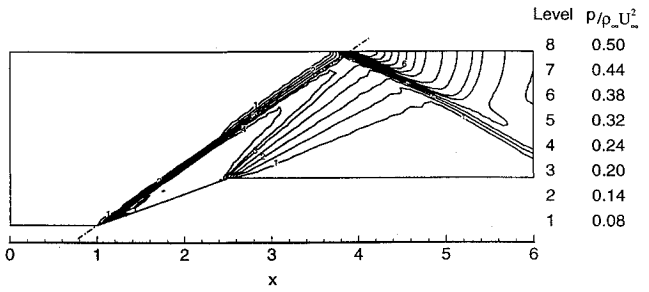

a) Pressure contour

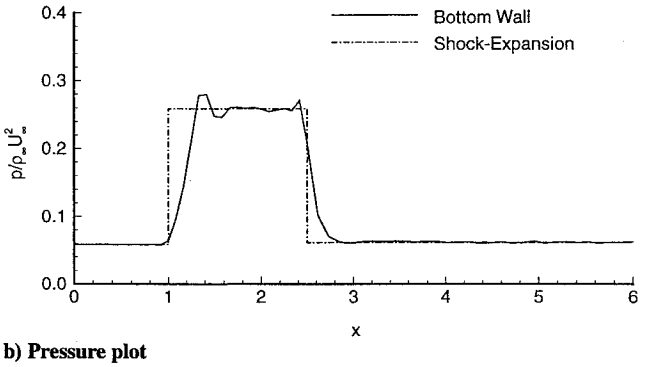

b) Pressure plot

Fig. 1 Inviscid flow, Mach 3.5, 20-deg ramp.

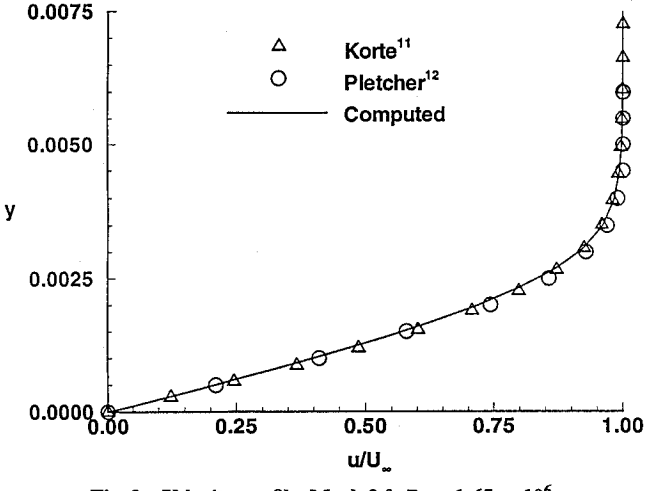

Fig. 2 Velocity profile, Mach 2.0, $Re = 1.65 \times 10^6$.

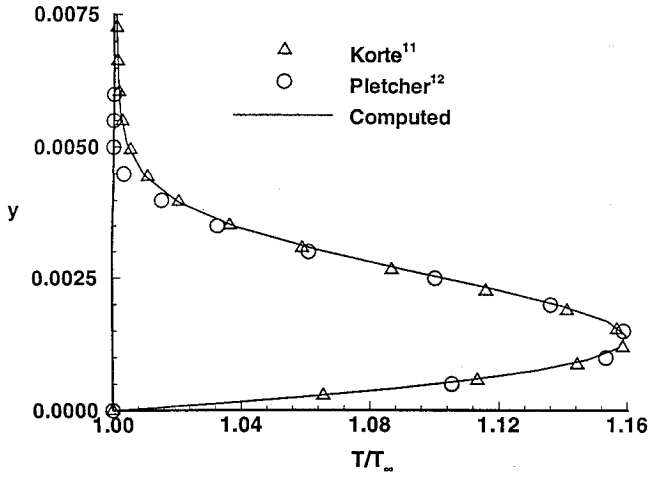

Fig. 3 Temperature profile, Mach 2.0, $Re = 1.65 \times 10^6$.

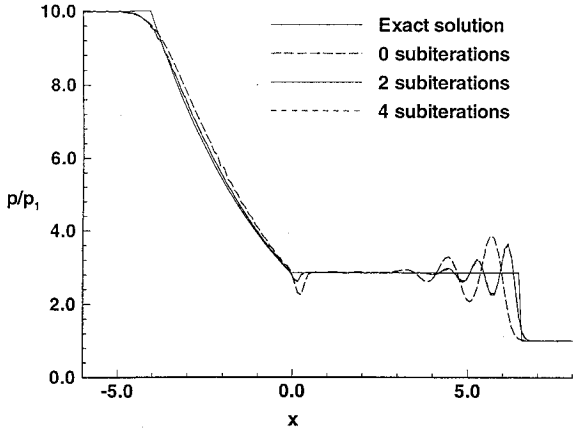

Fig. 4 Shock tube solution.

Validation Results

A Mach 3.5, two-dimensional inviscid flow, over a 20-deg compression ramp was computed, and the results compared with those predicted by the shock-expansion theory. The computation was performed on an evenly spaced 64×32 grid. Figure 1a shows a pressure contour plot with a dash-dotted line indicating the shock angle computed by the oblique shock solution superimposed on it. Figure 1b displays a pressure plot over the floor of the compression ramp and the shock-expansion solution superimposed on it. It can be seen that the solutions presented are in very good agreement. Korte[11] and Pletcher[12] presented computed solutions for a Mach 2.0 and Reynolds number 1.65×10^6 laminar flow over a flat plate. The former used a parabolized Navier–Stokes solver, and the latter numerically solved the boundary-layer equations. A comparison of those results with results computed with the present scheme are presented in Fig. 2 (velocity profiles) and Fig. 3 (temperature profiles) where a good agreement can be observed. To assess the effects of the subiteration procedure for a time-dependent problem, a solution for a shock tube problem was calculated. The initial pressure ratio was 10, with uniform temperature. For a grid with $\Delta x = 0.1$ and a time step $\Delta t = 0.05$, the computed solutions for 0, 2, and 4, subiterations are compared with the exact solution in Fig. 4. It can be seen that the dispersion errors characterized by the oscillation in front of the shock and the displacement error of the shock position are attenuated by the inclusion of subiterations. The same occurs with the spike in the numerical solution at the back of the expansion wave. The solution with four subiterations falls almost on top of the two subiteration solution, indicating that the rate of convergence within the pseudotime level is very fast, and only a few number of subiterations are needed.

Cavity Results

To the authors' knowledge, there are no published computational or experimental results for the unsteady, hypersonic flow over cavities. However, an experimental investigation of the mean flow characteristics of a Mach 7.3 hypersonic flow over cavities was reported by Hahn.[2] In this work he examined the effect of length-to-depth ratio and Reynolds number on the distribution of heat transfer and temperature and presented details of velocity distribution. The cavity was constructed on a large, hollow, axisymmetric body so as to produce near two-dimensional flow. For the range of Reynolds numbers investigated the separated flow was reported as laminar or transitional, hence no turbulence modeling was incorporated in the present code. The tests were conducted at a total temperature of 1100 K, wall temperature fixed at 300 K, and Reynolds numbers per meter, based on the conditions at the outer edge of the shear layer, of 1.033×10^6–4.085×10^6. Numerical calculations were performed for an outer edge Mach number of 6.3. The cavity length-to-depth ratios were 5.33, 8.0, and 10.67. Computational grids to solve numerically the three cavity dimensions were chosen after the evaluation of the effect of grid spacing on the numerical solution. Figure 5 shows the results of computed pressure distributions over the floor of a $L/D = 10.67$, Mach = 6.3, $Re/\text{m} = 4.085 \times 10^6$ cavity flow, for grid spacings being varied in the lengthwise and

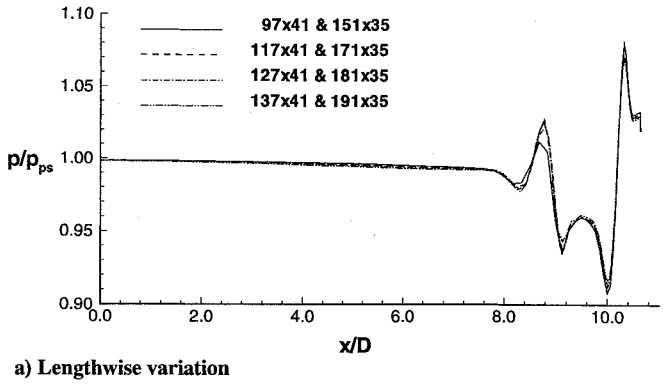

a) Lengthwise variation

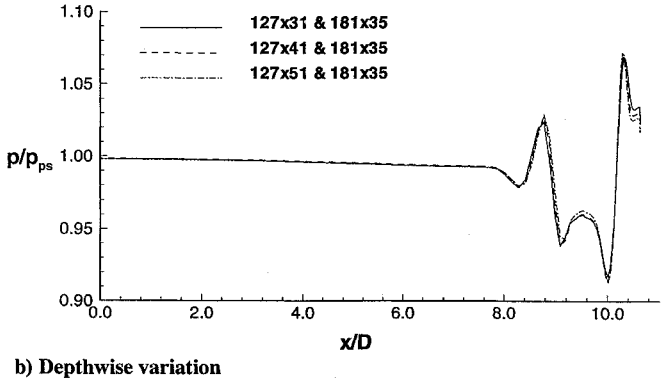

b) Depthwise variation

Fig. 5 Grid spacing comparison, L/D = 10.67, Mach 6.3, Re/m = 4.085 × 10^6.

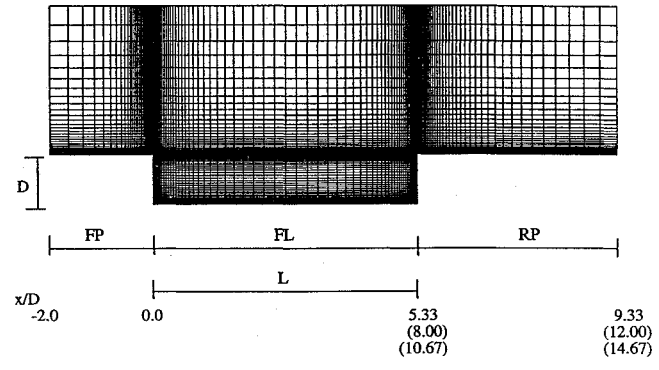

Fig. 6 Computational grid for the 5.33 length-to-depth ratio cavity.

depthwise directions. As Figs. 5a and 5b illustrate, increasing the lengthwise number of grid points above 127 and depthwise number of grid points above 41 inside the cavity results in no significant difference in the computational solutions. Based on these results and similar studies for the other length-to-depth ratio geometries, the computational grids employed in all computations hereafter were 81 × 41, 101 × 41, and 127 × 41, inside the cavity, and 132 × 35, 157 × 35, and 181 × 35, over the cavity, respectively, for the three cavities geometries. Figure 6 shows the computational grid for the 5.33 length-to-depth ratio cavity.

A comparison of the incoming velocity profile with experimental results, at an x/D station of −1.33 for the Reynolds number per meter of 2.116 × 10^6, is presented in Fig. 7. The agreement between the computed and experimental results is good. There are small differences at the boundary-layer edge and in outer edge values; this may be attributed to differences in determining the initial conditions for the calculations. A comparison of mean Mach number profiles at two stations within the cavity, presented in Fig. 8, shows a similar behavior. The computed result underpredicts the magnitude of the Mach number in the shear layer region when compared with the experimental data. Nevertheless, the general trends are very well cap-

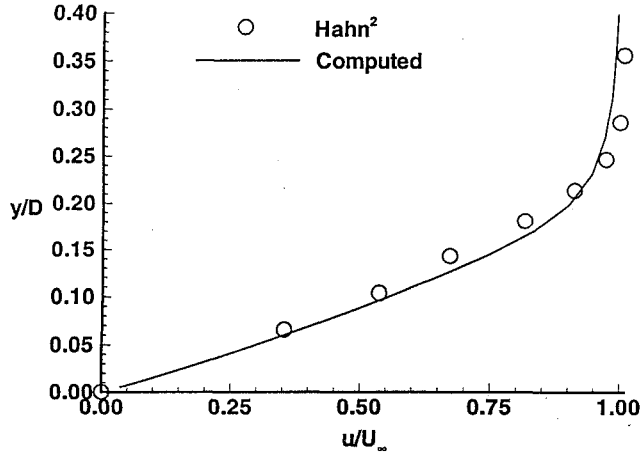

Fig. 7 Velocity profile at x/D = −1.33, L/D = 10.67, Mach 6.3, Re/m = 2.116 × 10^6.

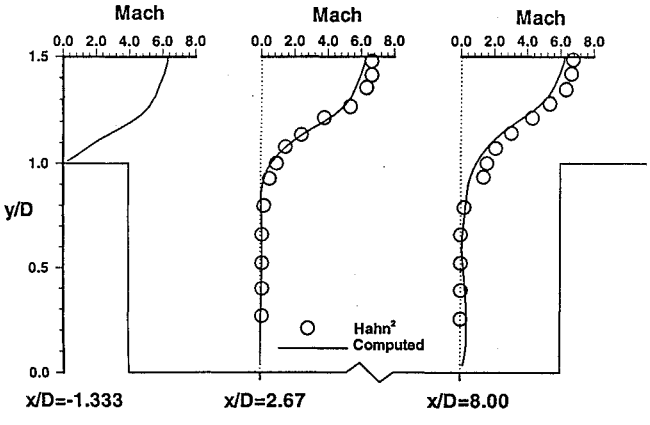

Fig. 8 Mach number profiles, L/D = 10.67, Mach 6.3, Re/m = 2.116 × 10^6.

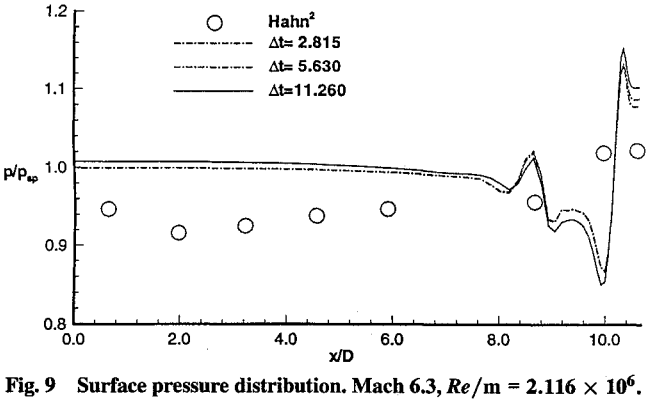

Fig. 9 Surface pressure distribution. Mach 6.3, Re/m = 2.116 × 10^6.

tured. A comparison of mean surface pressure is presented in Fig. 9. Computed results with three subiterations were obtained for three constant nondimensional time steps, Δt^* = 2.815, Δt^* = 5.63, and Δt^* = 11.26. As Fig. 9 shows, for a time step smaller than Δt^* = 5.63 there is no significant difference between the computed results. Hence, a time step of 5.63 was used to compute the cavity flows. The experimental data was nondimensionalized by a value just before separation (in his paper Hahn[2] did not present the value used in this nondimensionalization, however, experimental results for velocity, Mach number, and temperature, were presented at a station L/D = −1.33). The nondimensionalization value for pressure and heat transfer were taken as that at L/D = −1.33. The computed results, in the region just after the cavity forward wall, shows a uniform pressure, whereas a pressure drop is seen in the experimental results. Ahead of the cavity rearward wall the pressure drops in the computational results before rising to its stagnation value at the wall.

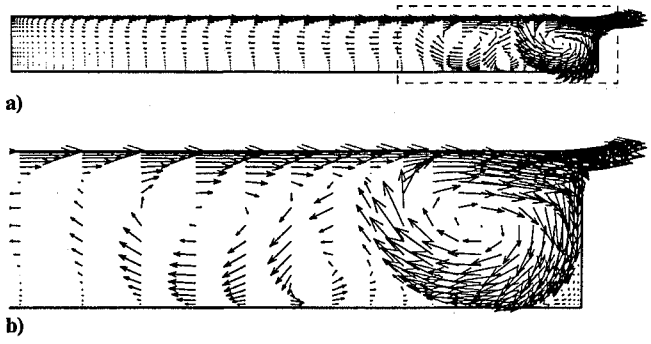

Fig. 10 Velocity vectors: a) L/D = 10.67 and b) close up of outlined region, Mach 6.3, $Re/m = 2.116 \times 10^6$. (Note: for sake of clarity only every other velocity vector is shown.)

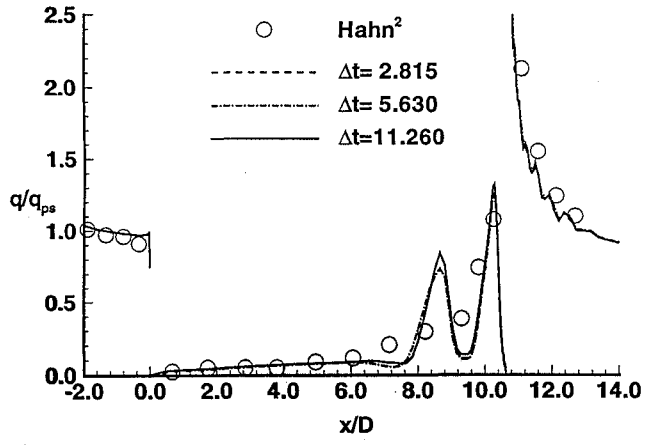

Fig. 11 Surface heat transfer ratio, Mach 6.3, $Re/m = 2.116 \times 10^6$.

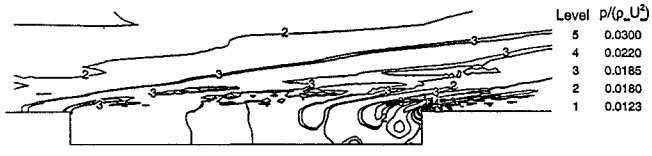

Fig. 12 Mean pressure contours, Mach 6.3, $Re/m = 2.116 \times 10^6$: L/D = 10.67.

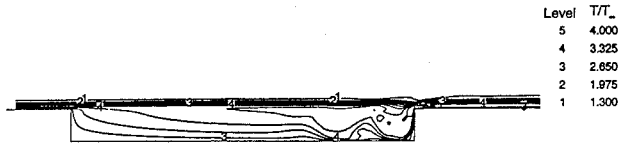

Fig. 13 Mean temperature contours, Mach 6.3, $Re/m = 2.116 \times 10^6$: L/D = 10.67.

The computed velocity vectors, shown in Fig. 10a, indicate that this drop in pressure is due to the presence of large vortical structures in this aft region of the cavity. The inadequate resolution in the experimental data does not capture this phenomenon. It is also of interest to note that a series of weaker vortex structures is located ahead of this primary vortex structure, Fig. 10b. Adjacent to the wall, a number of flow reversals are observed. In Fig. 11 the surface heat transfer rates over the front flat plate (FP), cavity floor (FL), and rear flat plate (RP) are compared with the experimental data. The agreement between the computed and experimental results is very good. Again, the computed results showed variations near the trailing edge of the cavity not found in the experimental data. The peaks are associated with the stagnant flow regions occurring between the vortex structures. Figure 11 also presents a comparison of the computed results for the three nondimensional time steps considered. This again shows that by reducing the time step below $\Delta t^* = 5.63$ there is no significant difference in the computed solutions.

Typical flowfield contours of the static pressure and temperature are shown in Figs. 12 and 13. The static pressure plot clearly shows a strong compression shock at the rearward wall where the separated shear layer reattaches. There are also pressure variations in the aft portion of the cavity, which are associated with the flow of the vortex structures. In the forward portion of the cavity the pressure is quite uniform and close to its freestream values. The temperature, on the other hand, shows large variations both within the cavity, especially near the cavity rearward wall, and across the shear layer. The localized surface heating effect due to the presence of the vortex structures is clearly seen. Upstream of these locations the surface temperature is quite uniform and the surface relatively cool. It is also evident that the separated shear layer completely bridges the cavity mouth.

The matrix of the nine cavity cases computed is shown in Table 1. The experimentally observed state of the separated shear layer is

Table 1 Hypersonic cavity test cases computed

L/D	Re/m ($\times 10^{-6}$)	Separated flow	Cavity
5.33	1.033	Laminar	Steady
	2.116	Transitional	Steady
	4.085	Transitional	Unsteady
8.00	1.033	Laminar	Steady
	2.116	Transitional	Steady
	4.085	Transitional	Unsteady
10.67	1.033	Laminar	Steady
	2.116	Transitional	Unsteady
	4.085	Transitional	Unsteady

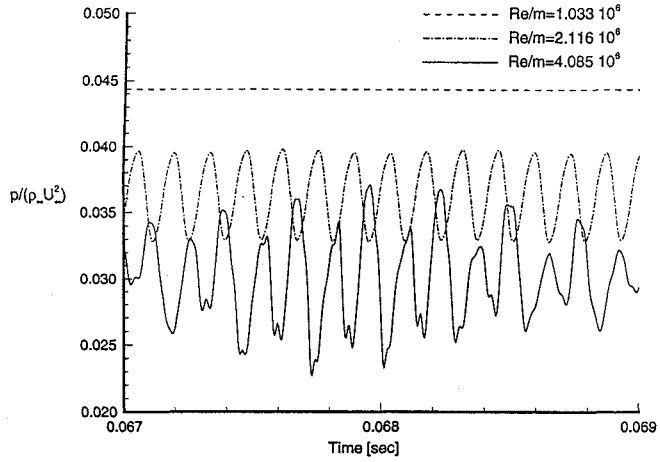

Fig. 14 Time history of pressure at the trailing edge of an L/D = 10.67 cavity, Mach 6.3, and Reynolds numbers per meter of 1.033×10^6, 2.116×10^6, and 4.085×10^6.

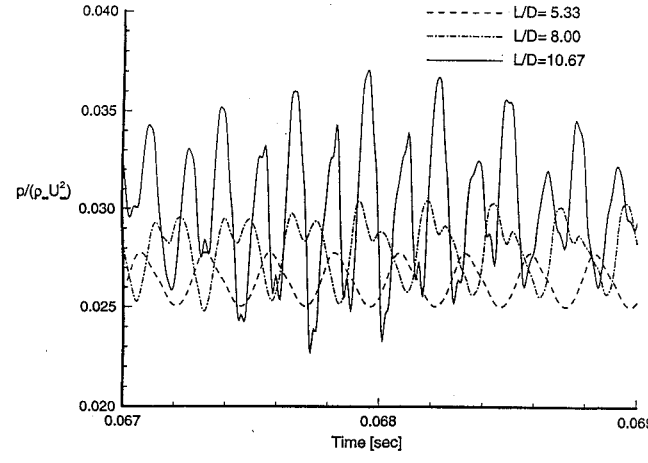

Fig. 15 Time history of pressure for the L/D = 5.33, 8.0 and 10.67 cavities, Mach 6.3, $Re/m = 2.116 \times 10^6$.

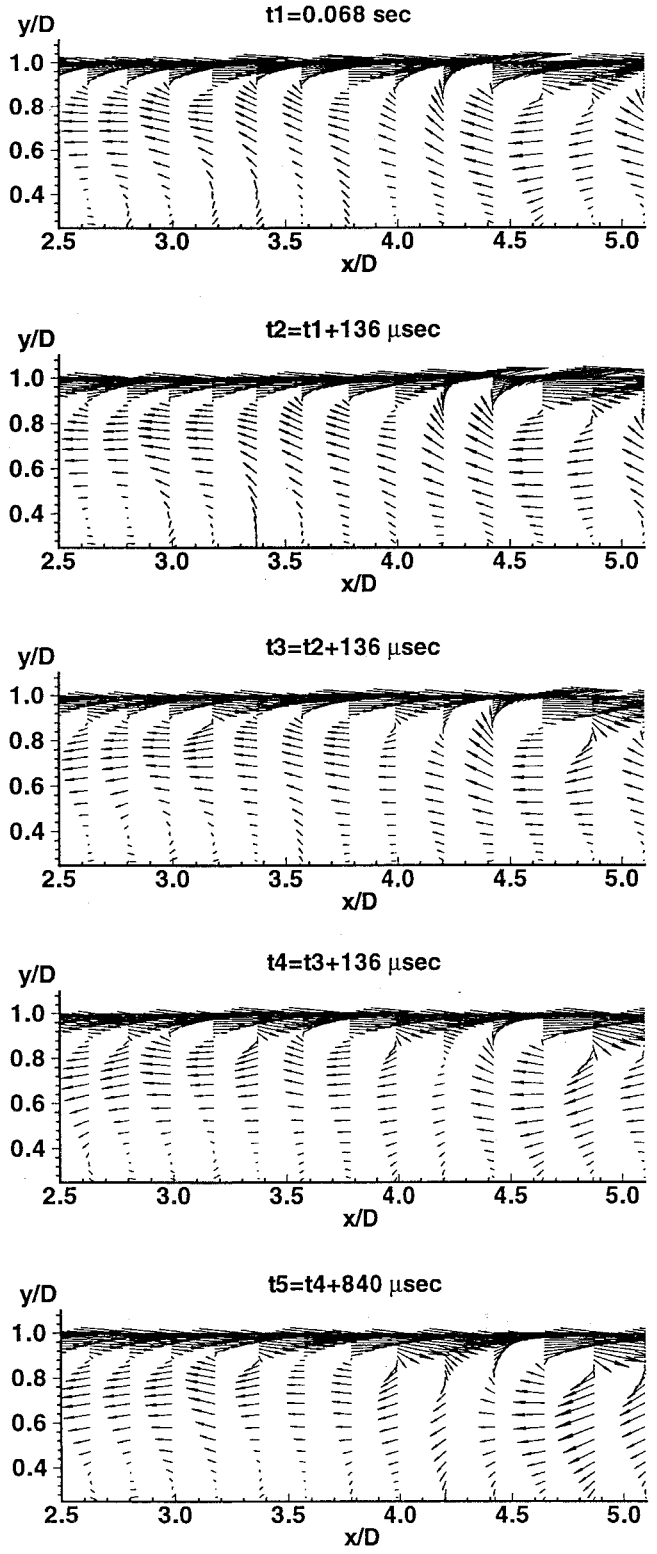

Fig. 16 Instantaneous velocity vectors, $L/D = 10.67$, Mach 6.3, $Re/\text{m} = 2.116 \times 10^6$.

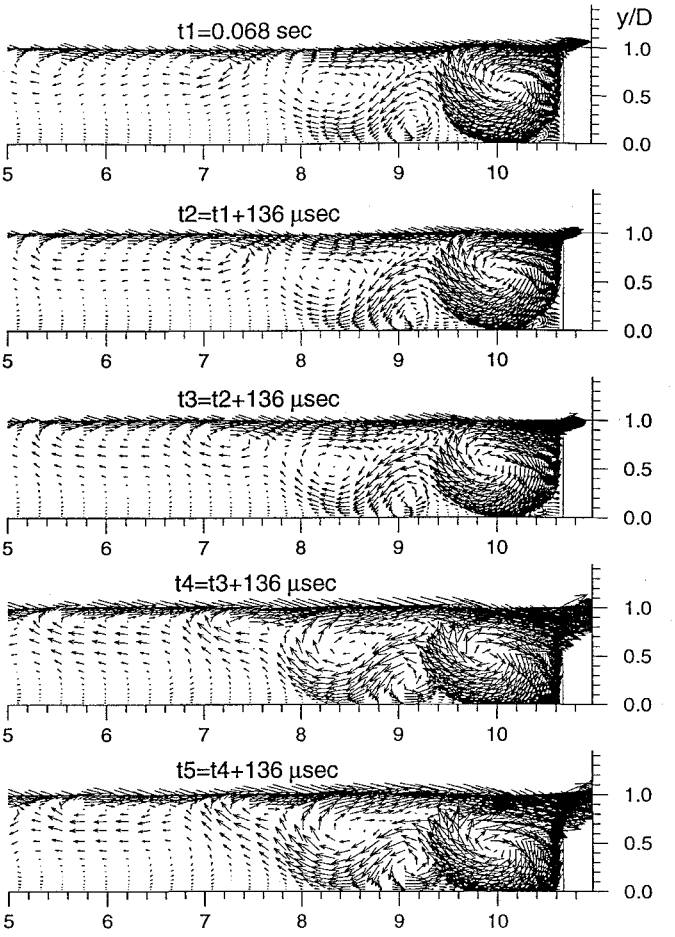

Fig. 17 Instantaneous velocity vectors at the trailing edge of an $L/D = 10.67$ cavity, Mach 6.3, $Re/\text{m} = 2.116 \times 10^6$.

shown, as is the computationally observed state of the cavity flow. For the cases examined, it was observed that the onset of unsteady cavity flow was a function of both the cavity length-to-depth ratio and the Reynolds number. For all cavity geometries considered, $L/D = 5.33$, 8.0, and 10.67, the laminar Reynolds number cavity flows were observed to be steady, whereas the transitional flows with Reynolds number of 4.085×10^6 showed an unsteady behavior. For the Reynolds number of 2.116×10^6 the two smaller cavities, $L/D = 5.33$ and 8.0, presented steady results, whereas the $L/D = 10.67$ cavity showed an unsteady behavior.

The effect of Reynolds number on the characteristics of the cavity flow can be seen in Fig. 14. The time histories of pressure at the rear cavity face for the $L/D = 10.67$ cavity and Reynolds numbers per meter of 1.033×10^6, 2.116×10^6, and 4.085×10^6 are shown. It can be observed that for the laminar Reynolds number the flow is steady, and for the two transitional Reynolds numbers an unsteady flow was observed. The mean pressure and the differences between the instantaneous and mean pressure decrease as Reynolds number increases and for the $Re/\text{m} = 4.085 \times 10^6$ case are as much as 25% of the mean pressure value. The character of the time history is typical of that observed in self-sustained cavity flows at lower speeds.

The effect of length-to-depth ratio on the oscillatory behavior of the cavity flow is shown in Fig. 15, where the pressure time histories for all cavity geometries with Mach number 6.3 and Reynolds number 4.085×10^6 are presented. It can be seen that the amplitudes of the pressure oscillations decrease with decreasing L/D ratio although they maintain a similar wave pattern. The basic unsteady character of the cavity flow is shown through the series of instantaneous velocity vectors in Figs. 16 and 17. Figure 16 shows the cavity flowfield close to the front face in $L/D = 10.67$ cavity. The shedding of vortices and their subsequent convection downstream in the shear layer are seen. An animation of the cavity flowfield showed that the shedding of these vortices was in phase with the arrival of pressure waves propagating upstream within the cavity. Figure 17 shows instantaneous velocity vectors at the trailing edge of the $L/D = 10.67$ cavity. The disturbances generated at the upstream cavity lip and characterized as the small vortices in the shear layer are seen. These small vortices merge with the larger vortical structures; the subsequent interaction of the vortical structures with the cavity rear wall generates pressure waves that propagate upstream. It is significant to note that no large vertical displacement of the large vortex is observed in the hypersonic flow as is seen in the lower speed cavity flows.[3]

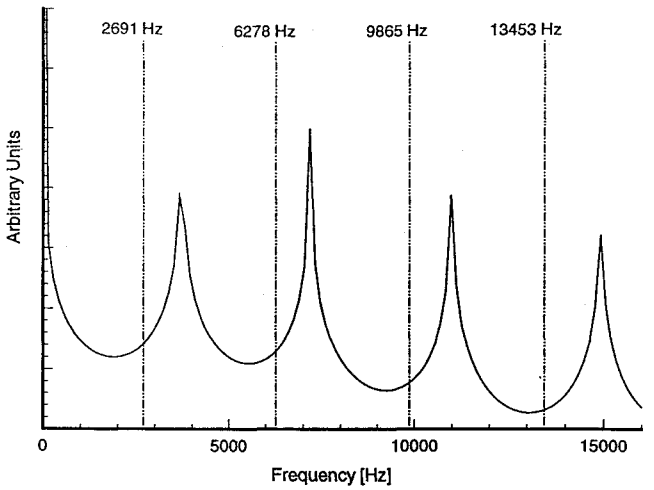

a) $L/D = 5.33$

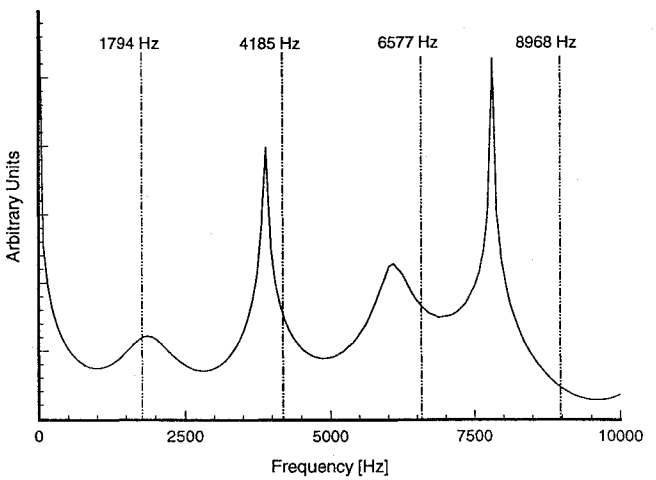

b) $L/D = 8.0$

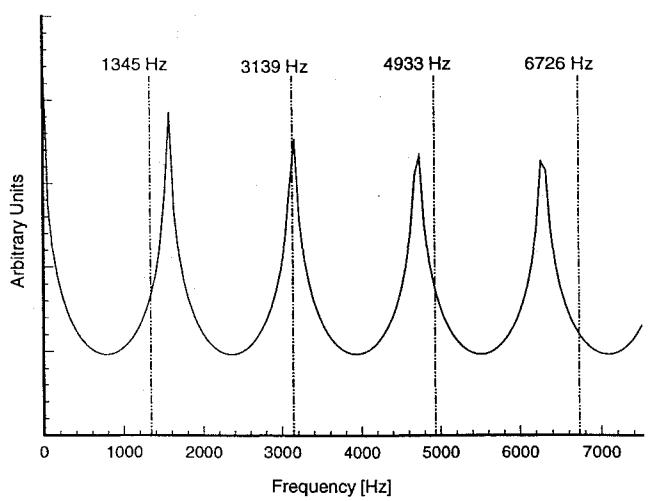

c) $L/D = 10.67$

Fig. 18 Frequency spectra of sound pressure level at the rear face cavity lip of Mach 6.3, $Re/m = 4.085 \times 10^6$ cavities.

Spectral analysis of the unsteady pressure time histories was conducted using an algorithm based on the maximum entropy method.[10] The frequency spectra of pressure data sampled at the rear face cavity lip for $Re/m = 4.085 \times 10^6$ of all cavity geometries are presented in Figs. 18a–18c. The computed spectral results are compared with frequencies predicted by the modified semiempirical formula of Rossiter as cited in Ref. 3. The computed spectra are in good agreement with the first four modes predicted by the semiempirical formula. Overall, it is observed the agreement is less good at relatively high frequencies compared to the lower frequencies.

Conclusions

A computational investigation of the hypersonic flow past a cavity has been accomplished. Time-accurate solutions of the nonreacting compressible Navier–Stokes equations have been obtained through the use of an implicit numerical algorithm; a subiteration procedure is implemented in the algorithm to achieve time accuracy. The numerical code is readily vectorizable, may be run at large CFL numbers, and thus is suited to the conduct of parametric studies. Laminar and transitional flows over three different cavity geometries were examined. The time-mean predictions showed good agreement with the available experimental data. Relatively large heat transfer rates and static pressure variations are observed in the rear part of the cavity. These gradients are associated with the large vortex structures in the rear of the cavity. For the high Reynolds number transitional flow, self-sustained flow oscillations were observed. The amplitudes of the oscillations are observed to increase with cavity length-to-depth ratio. These oscillations are associated with disturbances generated at the front of the cavity and pressure waves that propagate upstream from the rear of the cavity. However, unlike the lower speed cavity flows, no significant mass exchange is observed at the cavity rear. This work is the first phase of an effort to examine hypersonic cavity flows. In subsequent work, the effects of fine-scale turbulence will be included and the numerical algorithm extended to three dimensions.

Acknowledgments

The work of the first author was supported by the Instituto de Aeronáutica e Espaço/CTA; the work of the second author was supported in part by Grant NAGW-1331 to the Mars Mission Research Center. The North Carolina Supercomputing Center provided time on the Cray Y-MP computer. The authors gratefully acknowledge this support.

References

[1]Nestler, D. E., Saydah, A. R., and Auxer, W. L., "Heat Transfer to Steps and Cavities in Hypersonic Turbulent Flow," AIAA Paper 68-673, June 1968.

[2]Hahn, M., "Experimental Investigation of Separated Flow over a Cavity at Hypersonic Speed," *AIAA Journal*, Vol. 7, No. 6, 1969, pp. 1092–1098.

[3]Heller, H. H., and Bliss, D. B., "The Physical Mechanism of Flow-Induced Pressure Fluctuations in Cavities and the Concepts for their Suppression," AIAA Paper 75-491, March 1975.

[4]Kim, I, and Chokani, N., "Navier–Stokes Study of Supersonic Cavity Flowfield with Passive Control," *Journal of Aircraft*, Vol. 29, No. 2, 1992, pp. 217–223.

[5]Rizzetta, D. P., "Numerical Simulation of Supersonic Flow Over a Three-Dimensional Cavity," *AIAA Journal*, Vol. 26, No. 7, 1988, pp. 799–807.

[6]Yoon, S., and Kwak, D., "Implicit Navier–Stokes Solver For Three-Dimensional Compressible Flow," *AIAA Journal*, Vol. 30, No. 11, 1992, pp. 2653–2659.

[7]Matsuno, K., "A Time-Accurate Iterative Scheme For Solving the Unsteady Compressible Flow Equations," AIAA Paper 89-1992 CP, June 1989.

[8]Rogers, S. E., Kwak, D., and Kiris, C., "Steady and Unsteady Solutions of the Incompressible Navier–Stokes Equations," *AIAA Journal*, Vol. 29, No. 4, 1991, pp. 603–610.

[9]Simpson, L. B., and Whitfield, D. L., "Flux-Difference Split Algorithm for Unsteady Thin-Layer Navier–Stokes Solutions," *AIAA Journal*, Vol. 30, No. 4, 1992, pp. 914–922.

[10]Corke, T., Shakib, F., and Nagib, M., "Mode Selection and Phase Locking in Unstable Axisymmetric Jets," *Journal of Fluid Mechanics*, Vol. 223, Feb. 1991, pp. 253–311.

[11]Korte, J. J., "An Explicit, Upwind Algorithm for Solving the Parabolized Navier–Stokes Equations," Ph.D. Thesis, North Carolina State Univ., Raleigh, NC, 1989.

[12]Pletcher, R. H., "On a Calculation Method for Compressible Turbulent Boundary Layer Flows with Heat Transfer," AIAA Paper 71-165, Jan. 1971.